

RSC Advances



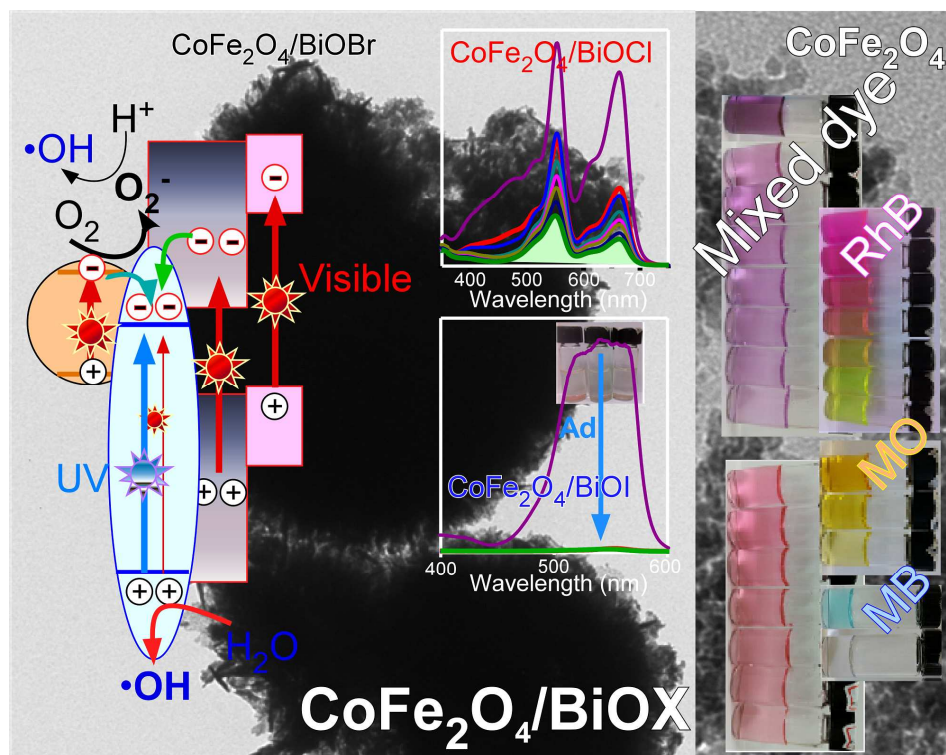
This is an *Accepted Manuscript*, which has been through the Royal Society of Chemistry peer review process and has been accepted for publication.

Accepted Manuscripts are published online shortly after acceptance, before technical editing, formatting and proof reading. Using this free service, authors can make their results available to the community, in citable form, before we publish the edited article. This *Accepted Manuscript* will be replaced by the edited, formatted and paginated article as soon as this is available.

You can find more information about *Accepted Manuscripts* in the [Information for Authors](#).

Please note that technical editing may introduce minor changes to the text and/or graphics, which may alter content. The journal's standard [Terms & Conditions](#) and the [Ethical guidelines](#) still apply. In no event shall the Royal Society of Chemistry be held responsible for any errors or omissions in this *Accepted Manuscript* or any consequences arising from the use of any information it contains.

Graphics Abstract



Magnetic $\text{CoFe}_2\text{O}_4/\text{BiOX}$ ($\text{X}=\text{Cl}$, Br and I) microflowers were tested for methyl orange, rhodamine B, methylene blue, and a mixed dyes

Recyclable magnetic CoFe₂O₄/BiOX (X=Cl, Br and I) microflowers for photocatalytic water treatments contaminated with methyl orange, rhodamine B, methylene blue, and a mixed dyes

Young In Choi,¹ Young-Il Kim,¹ Dae Won Cho,¹ Jung-Soo Kang,² K. T. Leung,² and Youngku Sohn^{1,*}

¹Department of Chemistry, Yeungnam University, Gyeongsan 38541, Republic of Korea
²WATLab and Department of Chemistry, University of Waterloo, Waterloo, Ontario N2L 3G1, Canada

Abstract

The recycling of photocatalysts and improving their activities by hybridizing two materials are important. Herein, nanosize ferromagnetic ($M_s = 62.3 \text{ emu} \cdot \text{g}^{-1}$) CoFe₂O₄ nanoparticles (NPs) were embedded into nanosize-assembled BiOX (X=Cl, Br and I) microflowers and examined by scanning electron microscopy, transmission electron microscopy, X-ray diffraction, UV-visible absorption spectroscopy, Fourier-transform infrared spectroscopy, and photoluminescence spectroscopy. The adsorption and photocatalytic performance of CoFe₂O₄/BiOX for methyl orange (MO), rhodamine B (RhB), methylene blue (MB), and a mixed dye (MO + RhB + MB) were examined under UV and visible light irradiation. The adsorption capacity of CoFe₂O₄/BiOI for RhB was 160 mg/g_{cat}, which is significantly larger than the <5mg/g_{cat} obtained for CoFe₂O₄/BiOCl and CoFe₂O₄/BiOBr. The photocatalytic activity was observed in the order of CoFe₂O₄/BiOBr < CoFe₂O₄/BiOCl < CoFe₂O₄/BiOI for RhB. Their adsorption and photocatalytic performances were also investigated with pure MO, pure MB and a mixed dye. MO in the mixed dye was the most easily removed by the catalysts under light exposure. Based on the scavenger tests, h⁺ and •O₂⁻ play major and minor roles in the photodegradation of the dyes, respectively. Although the •OH radical was formed for CoFe₂O₄/BiOBr and CoFe₂O₄/BiOCl, it has a much smaller role than the other active species.

* Corresponding author e-mail: youngkusohn@ynu.ac.kr
Tel: +82-53-810-2354; Fax: +82-53-810-4613

Key words: Magnetic CoFe₂O₄; BiOX photocatalysts; recycling; a mixed dye; photocatalytic dye degradation

1. Introduction

The development of efficient photocatalysts and adsorbents has been a major research focus for energy and the environment. As an environmental issue, removing pollutants present in water has been a persistent goal. In recent years, bismuth oxyhalides, BiOX (X=Cl, Br and I), have exhibited good adsorption/photocatalytic performance and been studied extensively.¹⁻¹⁰ A major advantage of these materials is the ease of band gap tuning between 1.7 eV and 3.4 eV by simply changing the (relative amount) halide ions.^{11,12} More recently, hybrid materials with BiOX have been developed to further increase the photocatalytic activity. The enormous hybrid materials include phthalocyanine (CuPc)/BiOCl,¹³ Bi₂S₃/BiOCl,¹⁴ Bi/BiOBr_xI_{1-x},¹⁵ BiOBr-g-C₃N₄,¹⁶ (Rh, Pd, Pt)/BiOX(Cl, Br, I),¹⁷ Ag-BiOBr,¹⁸ Ag/AgBr/BiOBr,¹⁹ Ag-BiOBr_xI_{1-x},²⁰ Bi₂₄O₃₁Cl₁₀,²¹ Bi₂WO₆,²² BiOCl/Bi₂O₂CO₃,²³ BiOI/BiPO₄,²⁴ Ag₃PO₄/BiOI,²⁵ Bi/BiOI,²⁶ BiOI-MWCNT,²⁷ Ti-BiOBr,^{28,29} and graphene-BiOBr.³⁰ The development of magnetic photocatalysts are of interest with the benefit of recyclability, even though in some cases, the catalytic activity is degraded after introducing magnetic materials into the host photocatalyst.³¹⁻⁴⁰ Magnetic SrFe₁₂O₁₉ was found to inhibit the growth of BiOCl along the [001] direction to expose the {001} facet. Furthermore, it induced visible light absorption (change in band gap from 3.3 eV to 2.8 eV after loading the magnetic material) and charge separation to increase photocatalytic MB degradation.³² Yao et al. prepared dandelion-like magnetic Fe₃O₄@C@BiOCl and Fe₃O₄@BiOCl composites. They reported that the surface area, adsorption capacity and photocatalytic activity were improved by introducing an interfacial carbon layer between Fe₃O₄ and BiOCl.³³ The total destruction of organic pollutants is important for eliminating pollution by secondary products. Zhang et al. solved this problem by synthesizing BiOBr@SiO₂@Fe₃O₄ microspheres through a multi-step synthesis process. They found only one main intermediate during the photocatalytic degradation of 2,2-bis(4-hydroxyphenyl) propane (BPA), where active h⁺ and •OH were mainly and partly involved in the direction oxidation, respectively.³⁴ For a photocatalytic reaction, the role of active species is very important and has been studied extensively using a number of methods, such as LC-MS,^{34,41,42} scavenger tests³⁴ and DMPO (5,5-dimethyl-1-pyrroline N-oxide) electron paramagnetic resonance (EPR) spin trapping techniques.^{21,31,43}

A literature summary (Supporting Information, Table S1)³²⁻⁴⁰ clearly showed the novelty of the present study. The previously reported BiOX-based magnetic photocatalysts include BiOCl–SrFe₁₂O₁₉,³² Fe₃O₄@C@BiOCl,³³ BiOBr@SiO₂@Fe₃O₄,³⁴ Fe₃O₄/BiOCl,^{35,36} Fe₃O₄@SiO₂@BiOBr,³⁷ BiOBr/Fe₂O₃,³⁸ BiOBr–ZnFe₂O₄,³⁹ and Fe₃O₄/BiOI.⁴⁰ However, all the catalysts^{32,33,35-40} were only tested with pure MO, RhB and MB dyes. There are no reports on a more complicated dye system such as mixed dyes. Because a real polluted area is complicated it is necessary to test a more complicated simulated dye system as presented in this study. The catalysts in the literatures were prepared with only a single BiOX matrix (for example, BiOCl, BiOBr or BiOI) and mainly tested under visible light. However, we prepared magnetic catalysts with three BiOX (for example, BiOCl, BiOBr and BiOI) matrices and tested both under UV and visible light conditions for systematic comparison and analysis.

In the present study, p-type BiOX was first hybridized with n-type CoFe₂O₄ to prepare magnetic CoFe₂O₄/BiOX (X=Cl, Br and I) composites for the purpose of recycling a photocatalyst and a simulated real water treatment. The catalysts were fully tested with MO, RhB and MB and a mixed dye (MO + RhB + MB) under UV and visible light. Hybridization of two different materials is an important strategy to increase a performance.^{32-40,44-48} A deeper understanding of the different roles of the photocatalysts to a more complicated dye system will be very important for developing a photocatalyst applicable to a more complicated system.

2. Experimental Section

2.1. Catalysts preparation

For the synthesis of CoFe₂O₄ nanoparticles (NPs), stoichiometric amounts (1:2 mole ratio) of Co nitrate and Fe nitrate were weighed and dissolved completely in ethylene glycol (EG) solvent. After heating the solution at 160°C for 1 hr, a 0.2 M Na₂CO₃ solution was added and the solution was stirred for 1 hr. Subsequently, the solution was cooled naturally and the products were filtered. For the synthesis of CoFe₂O₄/BiOX (X = Cl, Br and I) composites, CoFe₂O₄ NPs was first dispersed in EG solvent and a stoichiometric amount of Bi(NO₃)₃·5H₂O was added. The mole ratio of CoFe₂O₄/Bi was

fixed to 0.25. A stoichiometric amount of KX (X = Cl, Br and I) was then added. The Bi/X molar ratio was fixed to 1.0. The solution in a tightly capped Teflon bottle was placed at 120°C in an oven for 5 hrs. The final products were washed several times with deionized water and ethanol, and fully dried in an oven (80°C).

2.2. Catalysts characterization

The surface morphology of the hybrid samples was characterized by field-emission scanning electron microscopy (FE-SEM, Hitachi SE-4800). The crystal phase was analyzed by powder X-ray diffraction (XRD, PANalytical X'Pert Pro MPD) using Cu K α radiation ($\lambda = 0.154056$ nm) operated at 40 kV and 30 mA. Transmission electron microscopy (TEM) was used to examine the microstructure of a selected sample placed on a carbon-coated Cu grid. The diffuse UV-Vis absorption spectra were used to measure the band gaps of the powder samples using a SCINCO NeoSys-2000 double beam UV-Vis spectrophotometer. The Fourier-transform infrared (FT-IR, Thermo Scientific Nicolet iS10) spectra were obtained in attenuated total reflection (ATR) mode. The photoluminescence (PL) spectra of the powder samples were obtained using a SCINCO FluoroMate FS-2. Magnetic properties of the powder samples were examined using a MPMS SQUID magnetometer (Quantum Design, USA) with an applied magnetic field ranging from -70 to 70 kOe at room temperature. The Brunauer-Emmett-Teller (BET) surface areas for the powder samples were measured using a ChemBET TPR/TPD analyzer (Quantachrome Instruments, USA) equipped with a thermal conductivity detector.

2.3. Adsorption, photocatalytic activity and active species

For the BiOCl and BiOBr catalysts, a 20 mg/L RhB solution was used, while for BiOI, a 40 mg/L dye solution was used. For a mixed dye to test the photocatalytic performance of the BiOCl and BiOBr catalysts, 10 mg/L concentrations of MO, RhB and MB solutions were mixed. For a mixed dye to test the BiOI catalyst, 20 mg/L MO, RhB and MB solutions were mixed. For adsorption, 25 mg of a catalyst was dispersed into a

100 mL dye (RhB or the mixed dye) solution. The solution was fully stirred in the dark for 1 hour. The photocatalytic experiments were performed under visible and UV light with different light exposure times. The concentration of the dye solution was monitored using a Jasco V-530 UV–Vis spectrophotometer. A scavenger test was used to examine the roles of active $\cdot\text{OH}$ and $\cdot\text{O}_2^-$ species. Isopropyl alcohol (IPA) and benzoquinone (BQ) were added to the test solution as $\cdot\text{OH}$ and $\cdot\text{O}_2^-$ scavengers, respectively.^{49,50} To examine $\cdot\text{OH}$ radical formation over the catalysts, photoluminescence spectroscopy was performed using a terephthalic acid solution.³⁴ A catalyst was dispersed in the terephthalic acid solution and irradiated with UV or visible light for a specified time. The PL spectrum of the solution was taken at an excitation wavelength of 315 nm using a SCINCO FluoroMate FS-2 fluorometer.

3. Results and Discussion

3.1. Morphologies

Figure 1 presents SEM images of the $\text{CoFe}_2\text{O}_4/\text{BiOX}$ nano-assembled microflowers prepared in EG. The SEM images commonly showed distorted spheres with sizes of 1–3 μm . The assembled average sizes were in the order of $\text{CoFe}_2\text{O}_4/\text{BiOCl} < \text{CoFe}_2\text{O}_4/\text{BiOI} < \text{CoFe}_2\text{O}_4/\text{BiOBr}$. The magnified SEM images showed that the spheres differed slightly according to halide ions used and consisted of nanosize structures. The reported surface areas of bare BiOCl , BiOBr and BiOI microflowers were 17 m^2/g , 19 m^2/g and 61 m^2/g , respectively (Table 1).^{11,12} The similar surface areas for BiOCl and BiOBr may indicate that they had similar morphological structures as shown in Figure 1. Upon loading CoFe_2O_4 NPs, we observed the BET surface areas of 32.7 m^2/g , 30.9 m^2/g and 62.0 m^2/g for $\text{CoFe}_2\text{O}_4/\text{BiOCl}$, $\text{CoFe}_2\text{O}_4/\text{BiOBr}$ and $\text{CoFe}_2\text{O}_4/\text{BiOI}$, respectively (Table 1). The surface areas of BiOCl and BiOBr were substantially increased while that of BiOI showed no significant change after loading CoFe_2O_4 NPs. The BiOCl and BiOBr with smaller surface areas could be increased a lot further by loading with smaller size CoFe_2O_4 NPs.

Table 1. BET surface areas (m^2/g) of BiOX before and after loading CoFe_2O_4 NPs.

Catalysts	BiOCl	BiOBr	BiOI	ref.
before loading	17	19	61	[11,12]
After loading NPs	32.7	30.9	62.0	<i>This work</i>

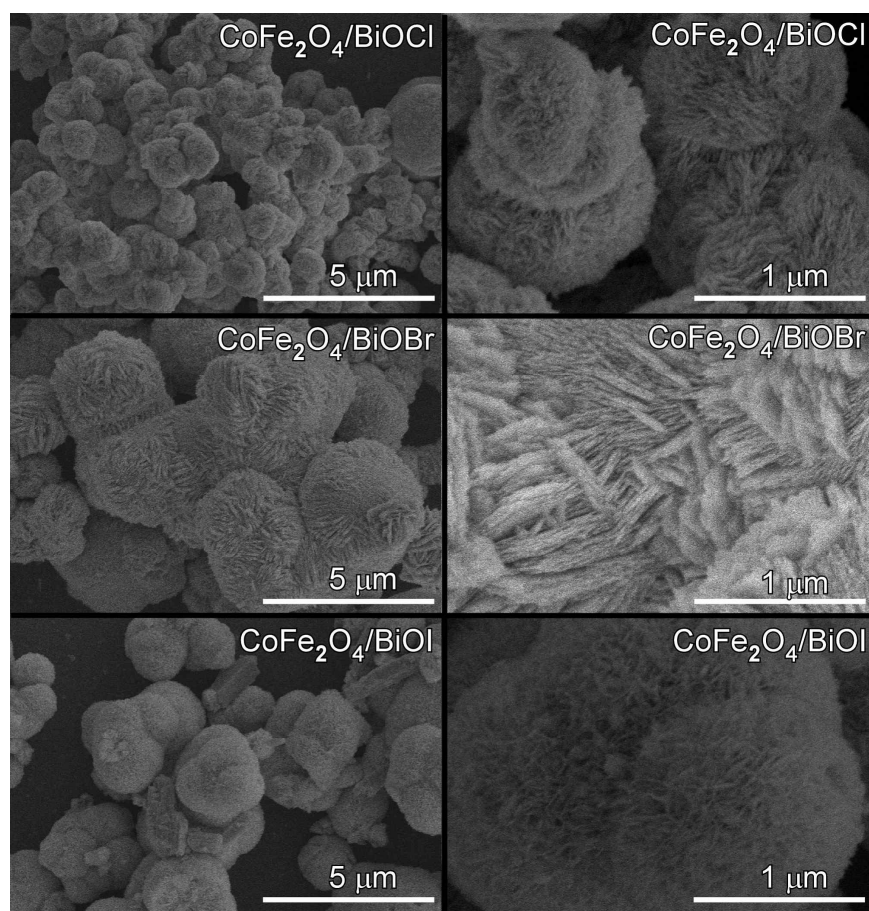
**Figure 1.** SEM images of $\text{CoFe}_2\text{O}_4/\text{BiOX}$ ($X=\text{Cl}$, Br and I) nano-assembled microflowers.

Figure 2 shows TEM images of the selected $\text{CoFe}_2\text{O}_4/\text{BiOI}$ microflowers and CoFe_2O_4 nanoparticles (NPs). The energy-dispersive X-ray (EDX) analysis confirmed the chemical species of the CoFe_2O_4 NPs and the hybrid materials (Supporting Information, Fig. S1). The magnetic CoFe_2O_4 NPs were very small with sizes of $< 5\text{nm}$. The 3D-microflowers were formed by the assembly of nanosize structures. The BiOX seeds were formed via the reaction, $\text{Bi}^{3+} + \text{X}^- + \text{H}_2\text{O} \rightarrow \text{BiOX} + 2\text{H}^+$. The nano-seeds assemble and grow into a larger sphere through Ostwald ripening.⁸ During this growth, the initially

dispersed much smaller NPs (unreactive to BiOX) became embedded into the μm -size BiOI microflowers to form hybrid $\text{CoFe}_2\text{O}_4/\text{BiOI}$ microflowers. Upon completion of the growth, BiOX microflowers generally showed $\{011\}$ and $\{020\}$ crystalline lattices, indicating higher percentage of $\{001\}$ facets.^{11,12} In the HRTEM image of Figure 2, a clear lattice fringe with a spacing of 0.199 nm corresponds to the (020) plane of tetragonal BiOI.¹²

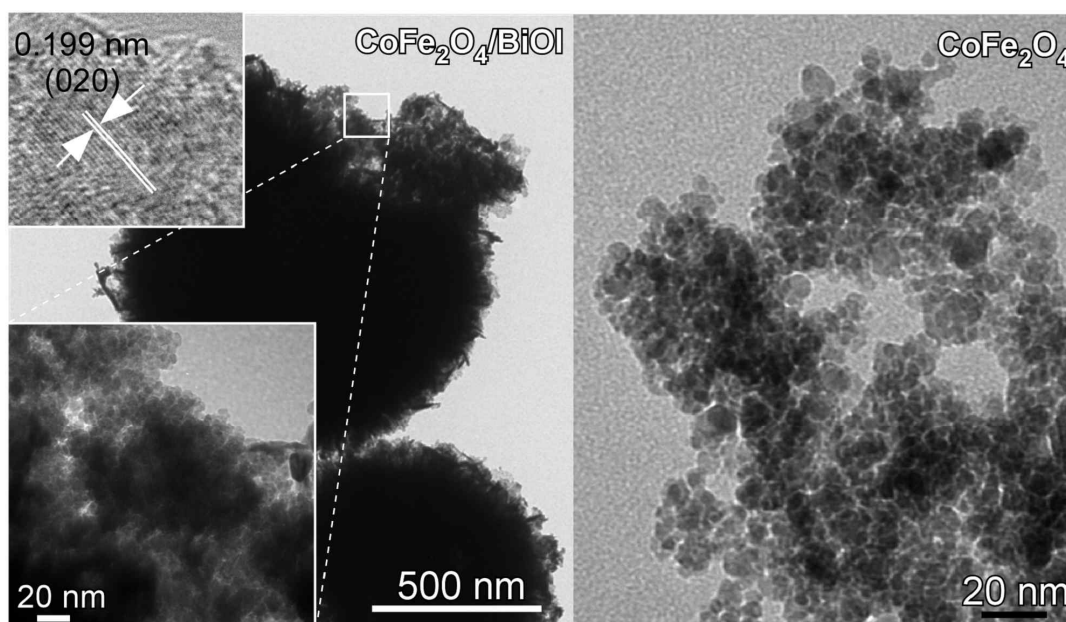
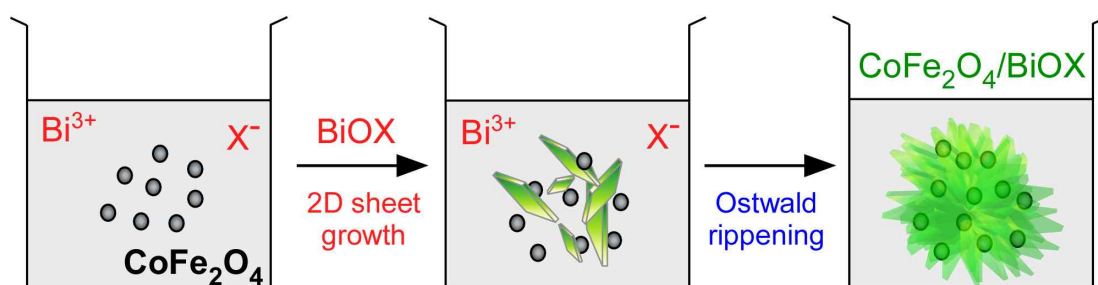


Figure 2. Typical TEM images of the $\text{CoFe}_2\text{O}_4/\text{BiOI}$ microflowers and CoFe_2O_4 nanoparticles. Left top inset shows the HRTEM image of the edge of BiOI.



Scheme 1. Growth mechanism of the hybrid materials

3.2. Crystal structures

Figure 3 shows the powder XRD patterns of CoFe_2O_4 NPs and $\text{CoFe}_2\text{O}_4/\text{BiOX}$ ($X = \text{Cl}, \text{Br}$ and I) microflowers. The XRD patterns of pure CoFe_2O_4 NPs were relatively weaker than those of the microflowers due to the lower crystallinity arising from the extremely small NP size ($<5\text{nm}$). The patterns matched those of cubic ($Fd-3m$) CoFe_2O_4 (JCPDS 3-0864). The peaks at $2\theta = 34.8^\circ$ and 60.5° were assigned to the (311) and (440) planes of the crystal structure. The other peaks included the (220), (222), (400), (422), and (511) planes. For the $\text{CoFe}_2\text{O}_4/\text{BiOX}$ ($X = \text{Cl}, \text{Br}$ and I) microflowers, the XRD peaks of CoFe_2O_4 NPs could not be discriminated clearly because of the smaller hybrid amount in the BiOX matrices and the weak XRD peaks of pure CoFe_2O_4 NPs. The XRD patterns of $\text{CoFe}_2\text{O}_4/\text{BiOCl}$ were similar to those of tetragonal ($P4/nmm$) BiOCl (JCPDS 1-085-0861). Three major peaks were observed at $2\theta = 25.9^\circ, 32.6^\circ$ and 36.4° , which were assigned to the (101), (110) and (102) planes of the tetragonal phase, respectively. The XRD patterns of $\text{CoFe}_2\text{O}_4/\text{BiOBr}$ matched those of tetragonal ($P4/nmm$) BiOBr (JCPDS 01-085-0862). Two major peaks at $2\theta = 31.7^\circ$ and 32.3° were assigned to the (102) and (110) planes, respectively. The XRD peak of the (101) plane was relatively weaker. For the $\text{CoFe}_2\text{O}_4/\text{BiOI}$ microflowers, the XRD peaks matched those of tetragonal ($P4/nmm$) BiOI (JCPDS 1-073-2062). Two major peaks were observed at $2\theta = 29.5^\circ$ and 31.8° corresponding to the (012) and (110) planes, respectively.

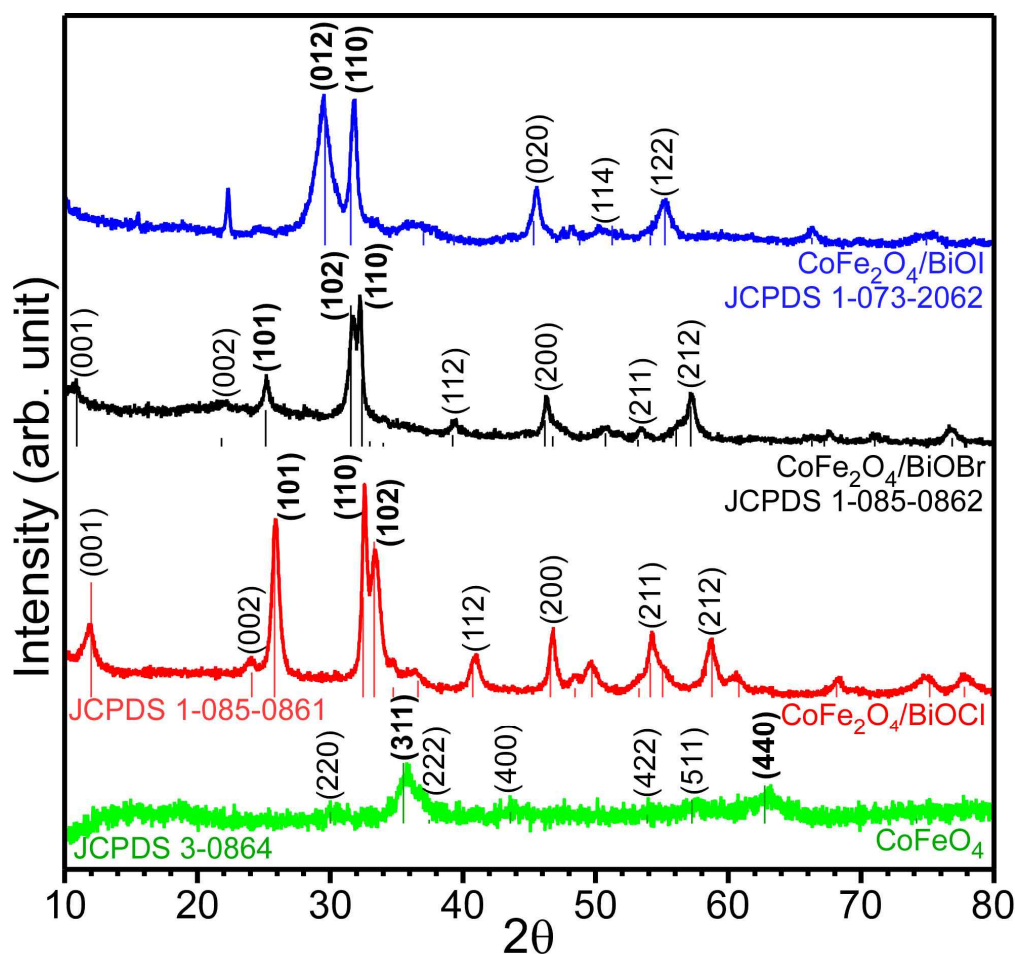


Figure 3. Power X-ray diffraction patterns of CoFe₂O₄ NPs, and CoFe₂O₄/BiOX (X= Cl, Br and I) microflowers.

3.3. Optical properties

Figure 4 shows the UV-Vis diffuse reflectance (DR) absorption spectra of CoFe₂O₄/BiOX (X= Cl, Br and I) microflowers. The Y-axis (absorbance) was obtained from the DR data using the Kubelka-Munk method. The sharp absorption edges (not shown) for bare BiOCl, BiOBr and BiOI microflowers were observed at 3.2, 2.8 and 1.8 eV, respectively. Upon loading the CoFe₂O₄ NPs, the absorption in the visible region were increased substantially and the colors of the samples became darker. We could expect a change in color and an increase in visible light absorption upon introducing black color CoFe₂O₄ NPs with a band gap of 1.2 eV. An increase in visible light

absorption facilitates photocatalytic activity under visible light.⁵¹ Although the visible light absorption of bare BiOCl and BiOBr microflowers was much lower than that of BiOI, the absorption became higher than BiOI after loading the CoFe₂O₄ NPs. Upon embedding CoFe₂O₄ NPs, the CoFe₂O₄/BiOX microflowers showed magnetic properties (as shown in the inset photos in Figure 4).

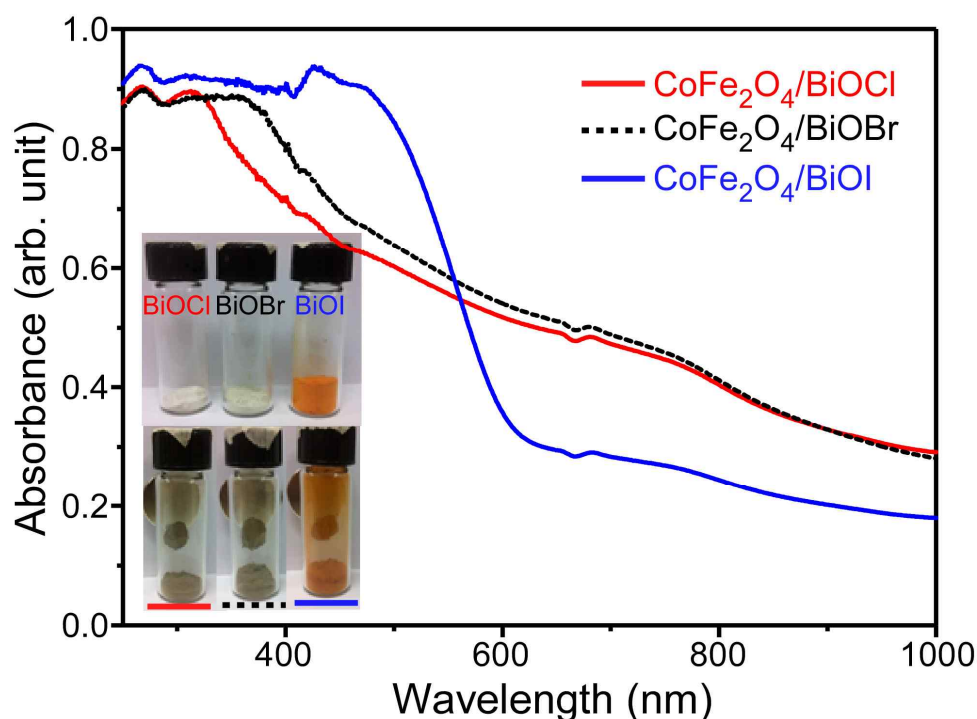


Figure 4. UV-visible diffuse reflectance absorption spectra of CoFe₂O₄/BiOX (X= Cl, Br and I) microflowers. The insets show photographs of the corresponding samples.

Figure 5 shows the photoluminescence (PL) spectra of CoFe₂O₄/BiOX (X= Cl, Br and I) microflowers taken at an excitation wavelength of 250 nm. The origin of the PL is the recombination of an electron and a hole. A higher the PL intensity indicates more recombination. Higher recombination indicates poor charge separation, generally leading to lower catalytic activity.⁵² The PL spectra of the three different samples were quite different with an intensity in the order of CoFe₂O₄/BiOI < CoFe₂O₄/BiOBr < CoFe₂O₄/BiOCl. As the band gap is larger (or the excitation energy is closer to the CB of a material), the PL becomes stronger. In other words, the band gap edge shifts to a longer wavelength as the halide ion is changed from Cl, Br to I. As a consequence, the PL peak

maximum is shifted to a longer wavelength. For the $\text{CoFe}_2\text{O}_4/\text{BiOCl}$ microflowers, broad regions were observed between 320 nm and 600 nm. For $\text{CoFe}_2\text{O}_4/\text{BiOBr}$, a broad peak at 460 nm was dominant. This was attributed to defects. For $\text{CoFe}_2\text{O}_4/\text{BiOI}$, the intensity decreased dramatically. A broad maximum was observed at 600 nm.

FT-IR spectra (Supporting Information, Fig. S2) were taken for $\text{CoFe}_2\text{O}_4/\text{BiOX}$ ($X = \text{Cl, Br and I}$) and BiOX microflowers. Several peaks were observed and the profiles were similar before and after loading the CoFe_2O_4 NPs. A broad peak at 3400 cm^{-1} and a sharper peak at 1600 cm^{-1} were attributed to the stretching and deformation vibrations of the adsorbed OH group.³²

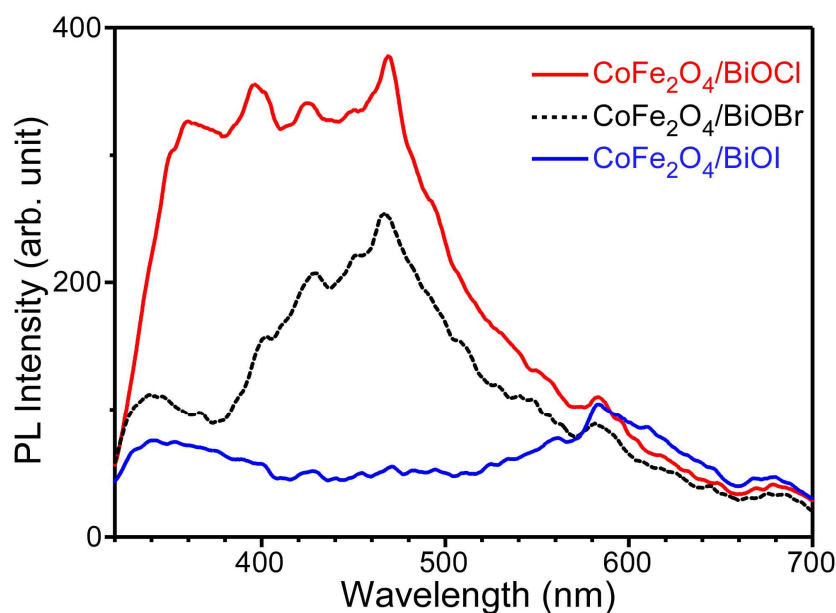


Figure 5. Photoluminescence spectra of $\text{CoFe}_2\text{O}_4/\text{BiOX}$ ($X = \text{Cl, Br and I}$) microflowers at an excitation wavelength of 250 nm.

3.4. Magnetic properties

The magnetic properties of CoFe_2O_4 NPs and $\text{CoFe}_2\text{O}_4/\text{BiOX}$ ($X = \text{Cl, Br and I}$) microflowers were examined by SQUID. Figure 6 shows the magnetization (M - H) curves measured with magnetic fields from -70 to 70 kOe at room temperature. The M - H curves commonly showed saturation magnetization (M_s). A saturation magnetization of $0.0623\text{ emu}\cdot\text{mg}^{-1}$ (or $62.3\text{ emu}\cdot\text{g}^{-1}$) was measured for CoFe_2O_4 NPs.

This value was in good agreement with the literature.⁴⁴ A magnetic hysteresis loop was observed (Supporting Information, Fig. S3), suggesting ferromagnetic behavior of the NPs. The hysteresis loop became significantly narrower for the hybrid materials. For $\text{CoFe}_2\text{O}_4/\text{BiOCl}$, $\text{CoFe}_2\text{O}_4/\text{BiOBr}$ and $\text{CoFe}_2\text{O}_4/\text{BiOI}$ microflowers, the magnetization values were decreased and measured to be 0.00747 , 0.0067 and $0.00621 \text{ emu}\cdot\text{mg}^{-1}$ (or 7.47 , 6.7 and $6.21 \text{ emu}\cdot\text{g}^{-1}$), respectively. The decrease in saturation magnetization is due to hybridization with non-magnetic BiOX ($X = \text{Cl}$, Br and I) materials.^{44,47} Although the magnetization of the hybrid sample was decreased^{44,47} the powder sample dispersed in a dye solution was easily (in a few seconds) attracted (or recycled) by a magnet (Supporting Information, Fig. S4).

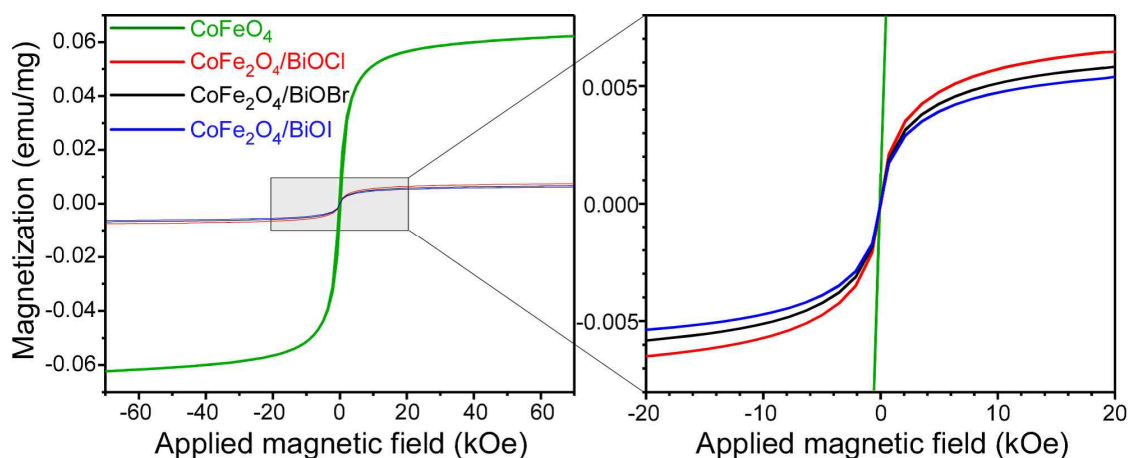


Figure 6. Magnetization (M–H) curves for CoFe_2O_4 NPs and $\text{CoFe}_2\text{O}_4/\text{BiOX}$ ($X = \text{Cl}$, Br and I) microflowers with applied magnetic fields from -70 to 70 kOe at room temperature.

3.5. Adsorption and photocatalytic activity of $\text{CoFe}_2\text{O}_4/\text{BiOCl}$ and $\text{CoFe}_2\text{O}_4/\text{BiOBr}$ for pure RhB

The adsorption and photocatalytic activities of $\text{CoFe}_2\text{O}_4/\text{BiOCl}$ microflowers for RhB were tested. Figure 7 shows the UV-Vis absorption spectra of RhB tested with the catalysts under visible (Figure 7A, 7B and 7C) and UV (Figure 7A1, 7B1 and 7C1) light irradiation. The roles of active $\cdot\text{O}_2^-$ and $\cdot\text{OH}$ radical species were also examined using a

scavenger test method. Benzoquinone (BQ) and isopropyl alcohol (IPA) were added as $\bullet\text{O}_2^-$ and $\bullet\text{OH}$ scavengers, respectively. RhB showed a broad UV-Vis absorption band at approximately 550 nm. The peak decreased after adsorption over the catalyst for 1 hour under dark conditions. Under visible light without a scavenger (Figure 7A), with increasing light exposure time, the UV-Vis absorption peak decreased substantially and the peak position shifted gradually to a shorter wavelength of 490 nm. The pink color of the original solution changed to a green color. This indicates that a secondary product had formed during the photocatalytic reaction of RhB over the catalyst. After visible light irradiation for 6 hrs, >95% of the RhB was degraded. The blue-shift in the peak for RhB is generally attributed to de-ethylation products by $\bullet\text{O}_2^-$ radical species.^{12,20,38} To confirm this, benzoquinone (BQ) was added as a $\bullet\text{O}_2^-$ radical scavenger and the photocatalytic experiments were performed (Figure 7B). Although the peak intensity decreased with increasing light exposure time, the peak position showed no change. Based on the results, it was concluded that the $\bullet\text{O}_2^-$ radical was involved in the photocatalytic reaction, but it did not affect the dye degradation greatly. To test the role of $\bullet\text{OH}$ radical species, IPA was added to the catalyst solution during photoirradiation (Figure 7C). The UV-Vis absorption peak decreased with increasing irradiation time, and changed its peak position. After adding IPA, the degradation rate was increased slightly due to the greater dispersion of the catalysts. The scavenger did not negate the photodegradation rate. This suggests that the $\bullet\text{OH}$ radical was not involved in the photocatalytic reaction. Li et al. also obtained a similar result for RhB over $\text{Fe}_3\text{O}_4/\text{BiOI}$ and reported that h^+ and $\bullet\text{O}_2^-$ were the major active species while $\bullet\text{OH}$ was a minor species for dye degradation.⁴⁰ Under UV irradiation, the degradation rate decreased and no shift in the peak position was observed (Figure 7A1). This suggests that the $\bullet\text{O}_2^-$ radical was not involved significantly in the photocatalytic reaction (Figure 7B1). After adding the $\bullet\text{OH}$ radical scavenger (Figure 7C1), IPA, a shift in the peak position under UV light irradiation with time was observed.

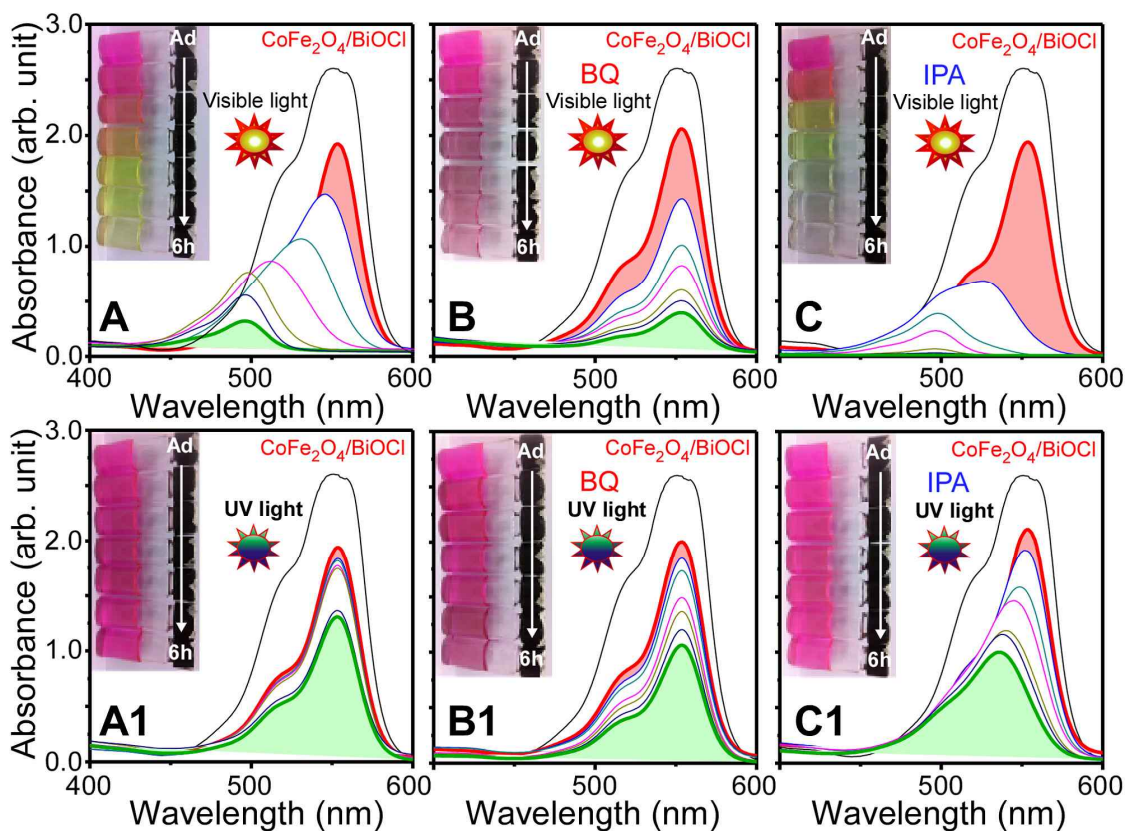


Figure 7. Adsorption (in dark) and photodegradation (under UV and visible lights) tests of RhB (20 mg/L, 100 mL) over 25 mg $\text{CoFe}_2\text{O}_4/\text{BiOCl}$ microflowers without (A and A1) and with scavengers of BQ (B and B1) and IPA (C and C1). The insets show the corresponding photographs displaying a change in the dye color with photodegradation time.

The adsorption and photocatalytic activity of the $\text{CoFe}_2\text{O}_4/\text{BiOBr}$ microflowers for RhB were examined by UV-Vis absorption spectroscopy (Supporting Information, Fig. S5). As discussed above, the catalysts were tested with and without active species scavengers under UV and visible light irradiation. The behaviors of the UV-Vis absorption spectra were similar to those of the $\text{CoFe}_2\text{O}_4/\text{BiOCl}$ microflowers. The adsorption performance of the $\text{CoFe}_2\text{O}_4/\text{BiOBr}$ microflowers was somewhat lower than that of $\text{CoFe}_2\text{O}_4/\text{BiOCl}$ microflowers. In addition, the photocatalytic activity was also lower than that of the $\text{CoFe}_2\text{O}_4/\text{BiOCl}$ microflowers. After adding BQ and IPA, similar results to those for the $\text{CoFe}_2\text{O}_4/\text{BiOCl}$ microflowers were obtained.

3.6. Adsorption and photocatalytic activity of $\text{CoFe}_2\text{O}_4/\text{BiOI}$ for pure RhB

Figure 8 displays the UV-Vis absorption spectra of RhB solution (40 mg/L) over $\text{CoFe}_2\text{O}_4/\text{BiOI}$ microflowers upon adsorption and with UV (Figure 8A) and visible (Figure 8B) according to the light exposure time. The adsorption capacity of the catalyst for RhB was extremely high (160 mg/g_{cat}). The high adsorption performance was attributed to a high surface area and electrostatic interactions between the catalyst and RhB.^{11,12,53} The negatively charged $\text{CoFe}_2\text{O}_4/\text{BiOI}$ surface may interact strongly with the positively charged RhB.^{11,12} Because of the high adsorption capacity, visible light is absorbed mainly by the uppermost adsorbed RhB. The UV absorption by the catalyst is also protected by the adsorbed RhB. Because of the UV protection, the adsorbed dye was photodegraded slowly (Figure 8A). As the visible light exposure time was increased, the extremely weak peak was shifted to a shorter wavelength (Figure 8B). This suggests that the RhB was de-ethylated by active $\cdot\text{O}_2^-$ species. Under UV light (Figure 8A), the shift in the peak position was much slower, indicating dull photodegradation. The catalyst sample after the UV light experiments was much darker than that after the visible light experiments.

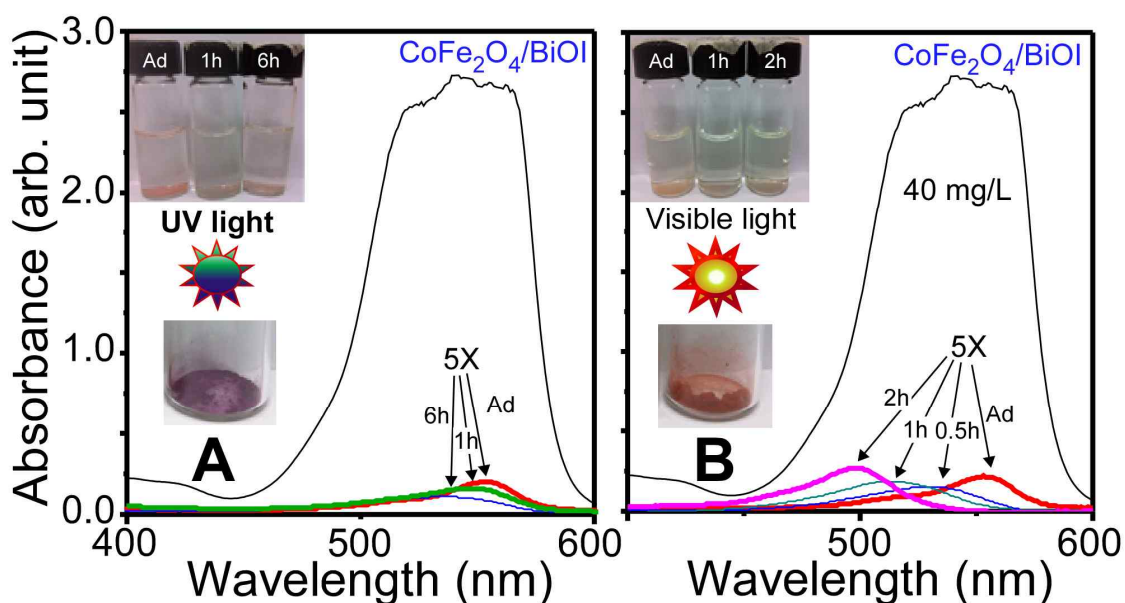


Figure 8. Adsorption (in dark) and photocatalytic dye degradation (A: under UV light, B: under visible light) of Rh B (40 mg/L, 100 mL) over 25 mg $\text{CoFe}_2\text{O}_4/\text{BiOI}$ microflowers.

The insets show photographs of the corresponding solutions showing a change in dye color with photoirradiation time. The weak peaks were multiplied by 5 \times .

3.7. Adsorption and photocatalytic activity of CoFe₂O₄/BiOX for pure MO and MB

We tested the adsorption and photocatalytic performances with pure MO and MB for comparison (Supporting Information, Fig. S6). Figure 9 displays adsorption (C/C_0) photocatalytic dye degradation (C_{6h}/C_{Ad}) performances for pure MO and MB over the CoFe₂O₄/BiOX (X=Cl, Br, I) microflowers under visible light irradiation. For pure MO, the adsorption and photocatalytic degradation performances showed an order of CoFe₂O₄/BiOCl < CoFe₂O₄/BiOBr < CoFe₂O₄/BiOI. For pure MB, the adsorption and photocatalytic degradation performances became an order of CoFe₂O₄/BiOBr < CoFe₂O₄/BiOCl < CoFe₂O₄/BiOI. Because the surface area of CoFe₂O₄/BiOI was larger than those of CoFe₂O₄/BiOCl and CoFe₂O₄/BiOBr (Table 1) it was expected that the adsorption and photocatalytic degradation performances were higher for the CoFe₂O₄/BiOI microflowers. For MO, the adsorption and photocatalytic degradation performances of CoFe₂O₄/BiOCl was poor than those of CoFe₂O₄/BiOBr although the surface area of CoFe₂O₄/BiOCl was somewhat larger than that of CoFe₂O₄/BiOBr. This reflects that other factors such as surface interactions play also important role in the adsorption and photocatalytic dye degradation.^{11,12,53} The adsorption capacities of CoFe₂O₄/BiOI for MO and MB were measured to be 24 and 21 mg/g_{cat}, respectively. This value was significantly smaller than that (160 mg/g_{cat}) for RhB, as mentioned above.

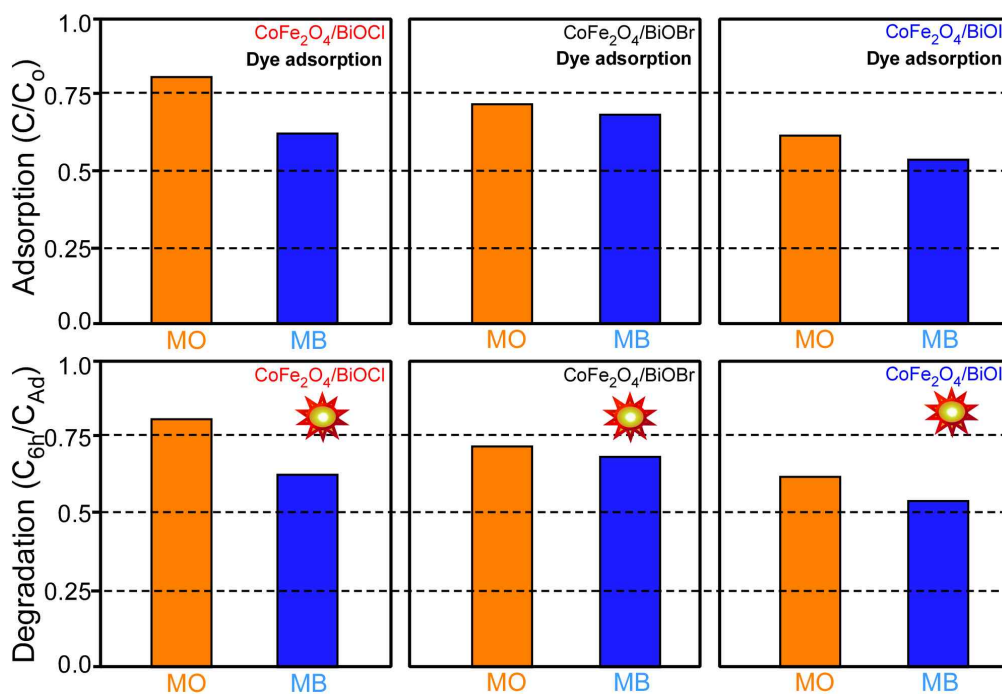


Figure 9. Adsorption (C/C_0) and photocatalytic dye degradation (C_{6h}/C_{Ad}) performances for pure MO and MB over the $\text{CoFe}_2\text{O}_4/\text{BiOX}$ ($X=\text{Cl, Br, I}$) microflowers. C_{Ad} and C_{6h} are the UV-Visible absorption intensities after adsorption and 6hrs visible light photoirradiation.

3.8. Adsorption and photocatalytic activity of $\text{CoFe}_2\text{O}_4/\text{BiOX}$ for a mixed dye

The adsorption and photocatalytic performances of the $\text{CoFe}_2\text{O}_4/\text{BiOCl}$ (Figure 10A and 10A1), $\text{CoFe}_2\text{O}_4/\text{BiOBr}$ (Figure 10B and 10B1), $\text{CoFe}_2\text{O}_4/\text{BiOI}$ (Figure 10C and 10C1) microflowers for a mixed dye (MO + RhB + MB) were tested under UV (Figure 10A, 10B and 10C) and visible (Figure 10A1, 10B1 and 10C1) light and the results are displayed in Figure 10. The mixed dye showed the absorptions of MO, RhB and MB as expected. The three peak positions of 450, 550 and 650 nm correspond to the MO, RhB and MB dyes, respectively. For the analysis, the three peak positions were selected and the heights of the peaks were examined. Upon adsorption of the mixed under the dark conditions, the UV-Vis absorption peak decreased. The adsorption performance of the mixed dye showed an order of $\text{CoFe}_2\text{O}_4/\text{BiOBr} < \text{CoFe}_2\text{O}_4/\text{BiOCl} \ll \text{CoFe}_2\text{O}_4/\text{BiOI}$. On the other hand, the three peaks over the catalyst were not evenly decreased. Figure 11

shows the adsorption performance of the $\text{CoFe}_2\text{O}_4/\text{BiOX}$ ($X = \text{Cl, Br and I}$) microflowers. In the mixed dye, MO showed the best adsorption over the $\text{CoFe}_2\text{O}_4/\text{BiOCl}$ (Figure 11A) and $\text{CoFe}_2\text{O}_4/\text{BiOBr}$ (Figure 11B) microflowers, whereas MB showed the best adsorption over the $\text{CoFe}_2\text{O}_4/\text{BiOI}$ microflowers (Figure 11C). MB was almost completely removed by the $\text{CoFe}_2\text{O}_4/\text{BiOI}$ microflowers. In contrast, RhB was the most poorly adsorbed on the $\text{CoFe}_2\text{O}_4/\text{BiOX}$ microflowers. Because of the relative difference in the adsorption performances over the catalysts, the mixed solutions tested with $\text{CoFe}_2\text{O}_4/\text{BiOBr}$ and $\text{CoFe}_2\text{O}_4/\text{BiOCl}$ became violet while that with $\text{CoFe}_2\text{O}_4/\text{BiOI}$ was pink after the adsorption in the dark condition.

Figure 12 displays the photodegradation rates of a mixed dye over $\text{CoFe}_2\text{O}_4/\text{BiOX}$ (Cl, Br, I) microflowers based on Figure 10. As the UV (Figure 12A, 12B and 12C) and visible (Figure 12A1, 12B1 and 12C1) light exposure times were increased, the UV-Vis absorption peaks were decreased. The catalytic activity for MO degradation under UV light (Figure 12A) was observed in the order of $\text{CoFe}_2\text{O}_4/\text{BiOI} < \text{CoFe}_2\text{O}_4/\text{BiOCl} < \text{CoFe}_2\text{O}_4/\text{BiOBr}$. For RhB (Figure 12B) and MB (Figure 12C), the catalytic activities were similar. For MO in the mixed dye under visible light (Figure 12A1), the catalytic activity showed a same order of $\text{CoFe}_2\text{O}_4/\text{BiOI} < \text{CoFe}_2\text{O}_4/\text{BiOCl} < \text{CoFe}_2\text{O}_4/\text{BiOBr}$. However, for RhB (Figure 12B1) and MB (Figure 12C1) under visible light irradiation, the order became $\text{CoFe}_2\text{O}_4/\text{BiOCl} \leq \text{CoFe}_2\text{O}_4/\text{BiOBr} < \text{CoFe}_2\text{O}_4/\text{BiOI}$. Based on the degradation rates of MO, RhB and MB over the photocatalysts in the mixed dye, MO was degraded most rapidly under visible light irradiation. The order of catalytic activity can be explained as follows. The catalytic activity showed no linear relationship with the BET surface area (Table 1). This indicates that other factors (e.g. exposed crystal facets, surface interactions, charge transfer, and energy level alignment) play more important role in the dye degradation than the surface area. It was reported that exposed crystal facets showed different catalytic reactivity for UV and visible light because the wavelength of incident light determines charge transfer direction. A charge transfer rate is very important for photocatalytic dye degradation.^{11,12} Different molecules are differently interacted with the different crystal facets and the energy levels (lowest unoccupied/highest occupied molecular orbitals and conduction/valence bands) are

differently realigned. The charge transfer rate is promoted by a well-aligned energy level (or a good interfacial wavefunction mixing).

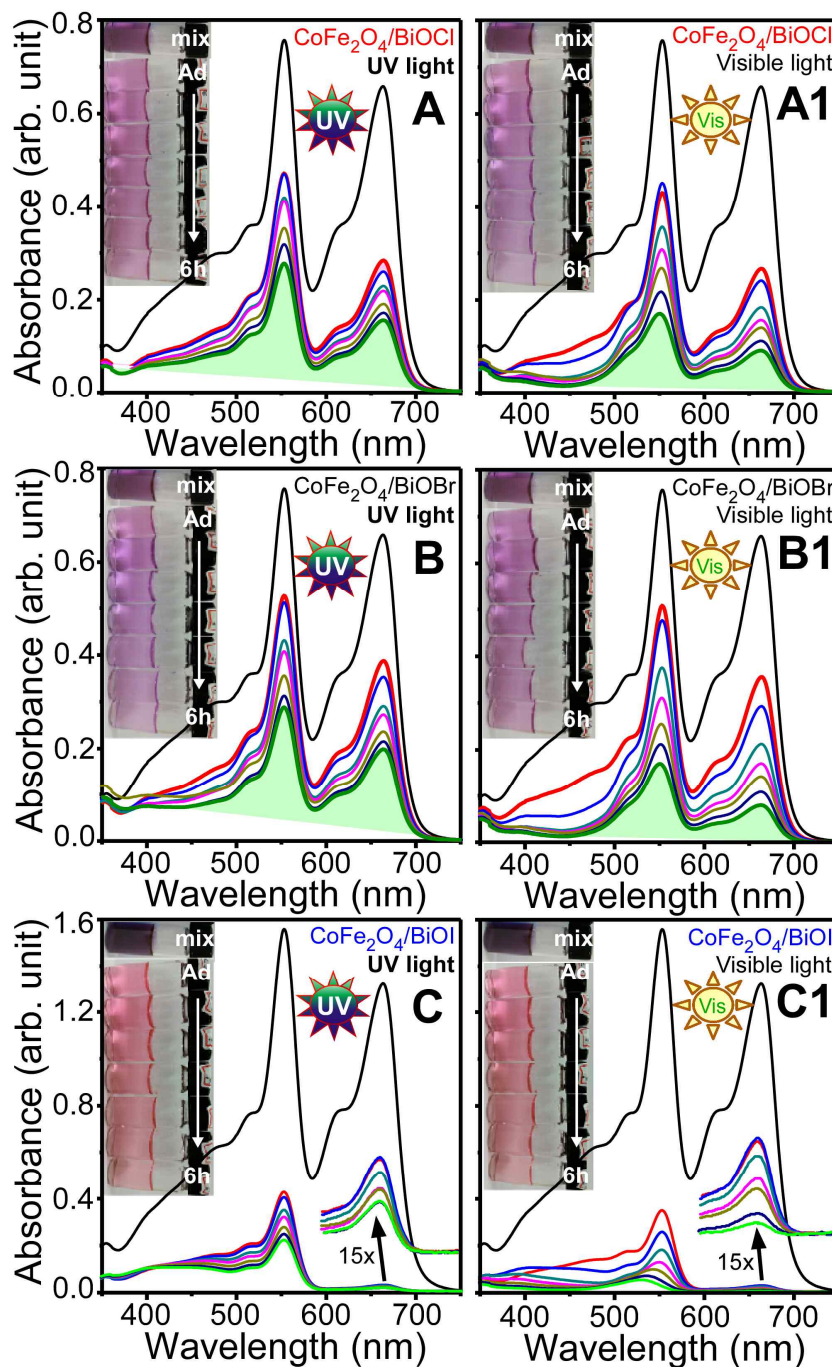


Figure 10. Adsorption (in dark) and photodegradation (under UV and visible lights) tests of the mixed dye (MO + RhB + MB) over 25 mg $\text{CoFe}_2\text{O}_4/\text{BiOX}$ ($X = \text{Cl}, \text{Br}$ and I) microflowers. For $\text{CoFe}_2\text{O}_4/\text{BiOCl}$ (A and A1) and $\text{CoFe}_2\text{O}_4/\text{BiOBr}$ (B and B1), a dye

mixed with the three dyes with a concentration of 10 mg/L (=ppm) was used. For $\text{CoFe}_2\text{O}_4/\text{BiOI}$ (C and C1), a dye mixed with the three dyes with a concentration of 20 mg/L was used. The insets show photographs of the corresponding dye solutions as a function of the photodegradation time. The weak peaks were multiplied by 15.

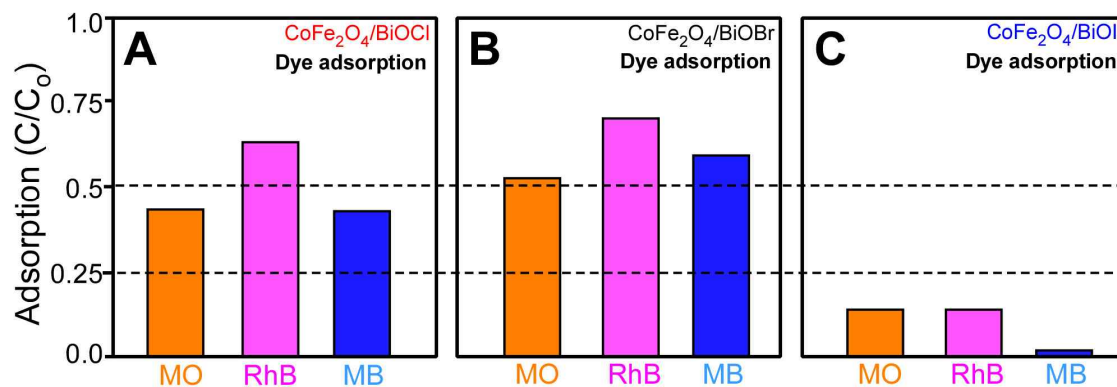


Figure 11. Adsorption performance of the mixed dye (MO + RhB + MB) over the $\text{CoFe}_2\text{O}_4/\text{BiOCl}$ (A), $\text{CoFe}_2\text{O}_4/\text{BiOBr}$ (B) and $\text{CoFe}_2\text{O}_4/\text{BiOI}$ (C) microflowers.

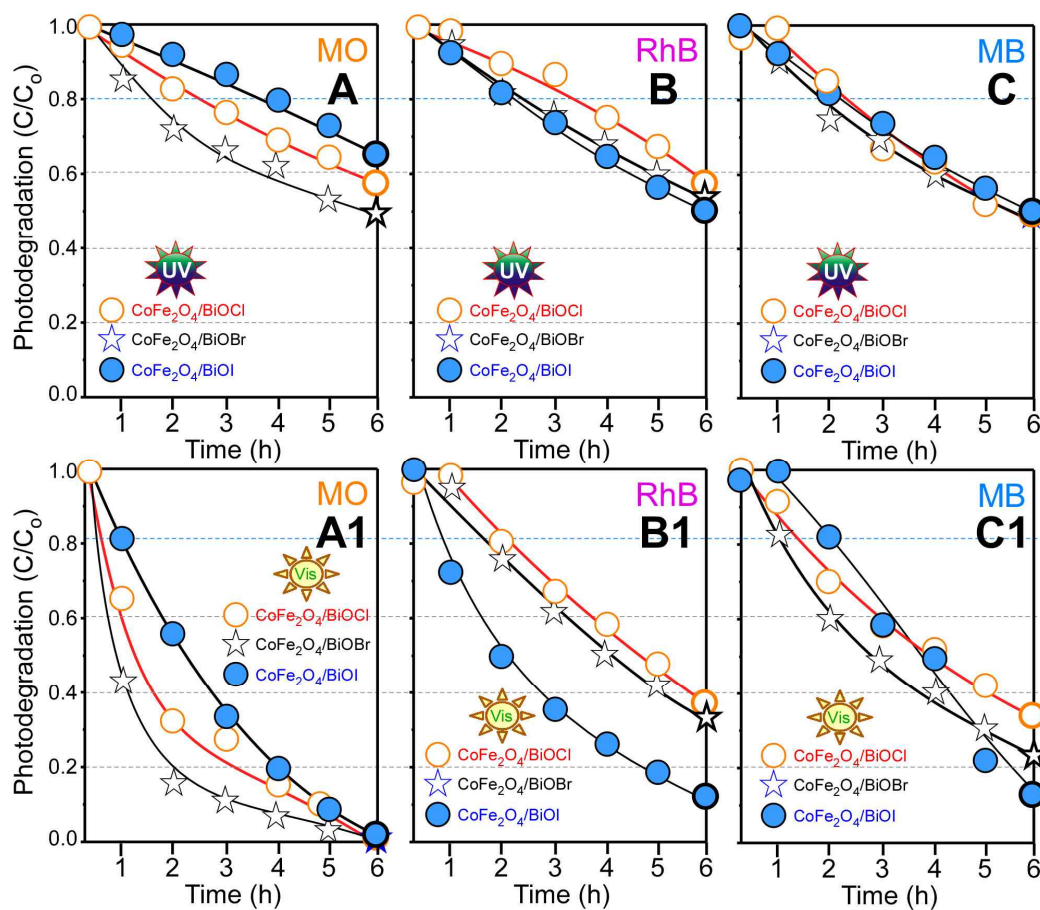


Figure 12. Photodegradation rates of MO (A and A1), RhB (B and B1) and MB (C and C1) dyes in the mixed dye over CoFe₂O₄/BiOX (Cl, Br, I) microflowers under UV (top: A, B and C) and visible (bottom: A1, B1 and C1) light.

3.9. •OH radical formation probed by PL

The formation of •OH radicals over the catalysts during photoirradiation was probed by photoluminescence (PL) spectroscopy.³⁴ A catalyst is dispersed in a terephthalic acid (TA) solution and irradiated with UV (or visible) light while stirring. When a •OH radical is formed, TA reacts with the radical to form 2-hydroxyterephthalic acid, which emits a blue emission signal at approximately 425 nm. The intensity of the emission peak reflects the amounts of •OH radical produced during photoirradiation. Figure 13 shows the photoluminescence spectra taken after UV and visible light irradiation for 6 hrs. For CoFe₂O₄/BiOCl and CoFe₂O₄/BiOBr, the photoluminescence signal was increased significantly under UV irradiation, while the intensity under visible light was observed to be weaker. Zhang et al. also reported •OH radical formation under visible light for BiOBr@SiO₂@Fe₃O₄ microflowers.³⁴ For CoFe₂O₄/BiOI, no photoluminescence signal was observed under UV and visible light irradiation, indicating no •OH radical formation. Under UV light, the PL intensity for CoFe₂O₄/BiOBr was stronger than that for CoFe₂O₄/BiOCl. Under visible light irradiation, the intensities became similar.

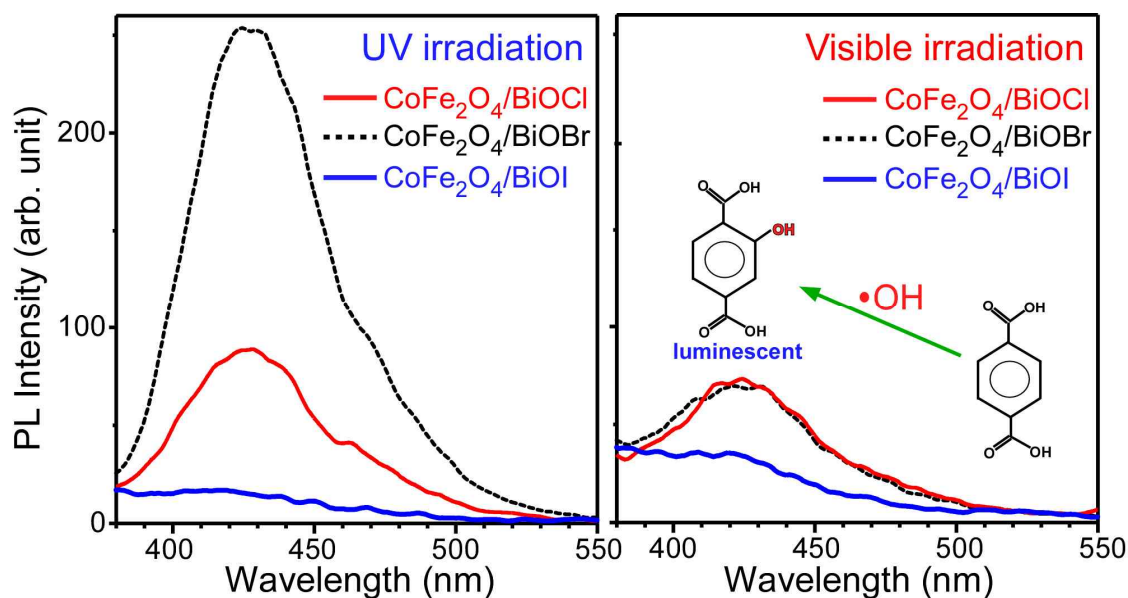
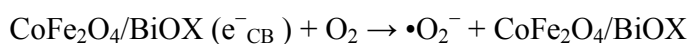
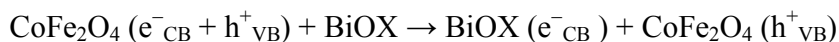
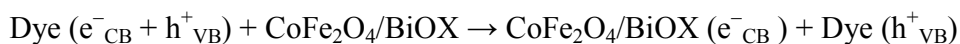
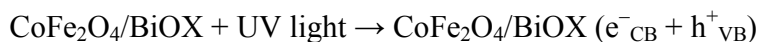
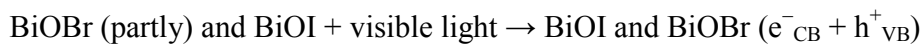
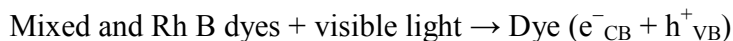


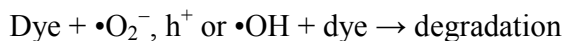
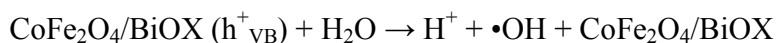
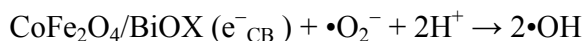
Figure 13. Photoluminescence spectra of a terephthalic acid solution over the $\text{CoFe}_2\text{O}_4/\text{BiOX}$ ($X = \text{Cl}, \text{Br}$ and I) microflowers after UV (left) and visible (right) light irradiation for 6 hrs.

3.10. Photocatalytic mechanism and reliability/stability

The following photocatalytic degradation mechanism (as shown in Figure 14) can be proposed based on the present results and the literature.^{41,49-51,54-63} Three active species of hydroxyl radicals ($\bullet\text{OH}$), superoxide radicals ($\bullet\text{O}_2^-$) and holes (h^+) act as the major species for photocatalytic dye degradation.

Under UV or visible light irradiation:





Under visible light irradiation, the dye and the catalyst (with a lower band gap) absorb light to create an electron and a hole in the conduction and valence bands (CB and VB) of the materials, respectively. BiOI ($E_g = 1.8$ eV) and BiOBr ($E_g = 2.8$ eV) strongly and partly absorb visible light, respectively. BiOCl (3.2 eV) does not absorb visible light. The electron in the CB of the dye transfers to that of the BiOX material. This is often called a dye-sensitized mechanism. CoFe_2O_4 ($E_g = 1.2$ eV) also absorbs visible light well,⁶⁴ and electron in the CB of the CoFe_2O_4 transfers to that of BiOX. The electron in the CB is captured by adsorbed oxygen (an electron acceptor) to produce active $\bullet\text{O}_2^-$ species. Active $\bullet\text{OH}$ radicals can be produced by the reactions of $\bullet\text{O}_2^-$ species and electron (e^-_{CB}) or water and hole (h^+_{VB}). The active $\bullet\text{O}_2^-$, h^+ and $\bullet\text{OH}$ species will consequently degrade the adsorbed dye. The $\text{CoFe}_2\text{O}_4/\text{BiOI}$ microflowers showed no creation of $\bullet\text{OH}$ radical species while $\text{CoFe}_2\text{O}_4/\text{BiOCl}$ and $\text{CoFe}_2\text{O}_4/\text{BiOBr}$ formed some $\bullet\text{OH}$ radical species. Under visible light, the amount formed was very small compared to that under visible light. Based on the results discussed above, the role of the $\bullet\text{OH}$ radical was much weaker than that of the other active species. The role of $\bullet\text{O}_2^-$ species depends on the amount of oxygen dissolved in the dye solution.⁶⁵ In the present study, $\bullet\text{O}_2^-$ species were weakly involved in the photocatalytic reaction. Consequently, h^+ plays a major role in dye degradation, as reported for the $\text{Fe}_3\text{O}_4/\text{BiOI}$ catalyst.⁴⁰ Under UV irradiation, the catalysts mainly absorb incident UV light and directly create an electron and hole in the CB and VB of the $\text{CoFe}_2\text{O}_4/\text{BiOX}$ catalysts, respectively. The electrons in the CBs of the catalysts commonly initiate the creation of active species. Therefore, the catalytic activities were not much different than those found under visible light, as shown in Figure 11.

Finally, we tested reliability and stability of the catalyst samples after the photocatalytic dye degradation experiments. We found that the crystal structure of the catalyst samples showed no change after photocatalytic dye degradation experiments. This indicates that the catalysts were very stable based on the XRD patterns (Supporting Information, Fig. S7). We tested the reusability of the catalysts samples, and found that

about 80% of the initial performance was obtained in the second cycle. It took more time to completely photo-dissociate dye in a solution (Supporting Information, Fig. S8). This is due to some aggregation of the magnetic catalyst particles. However, in the third cycle the catalytic activity showed no significant decrease compared with the second cycle.

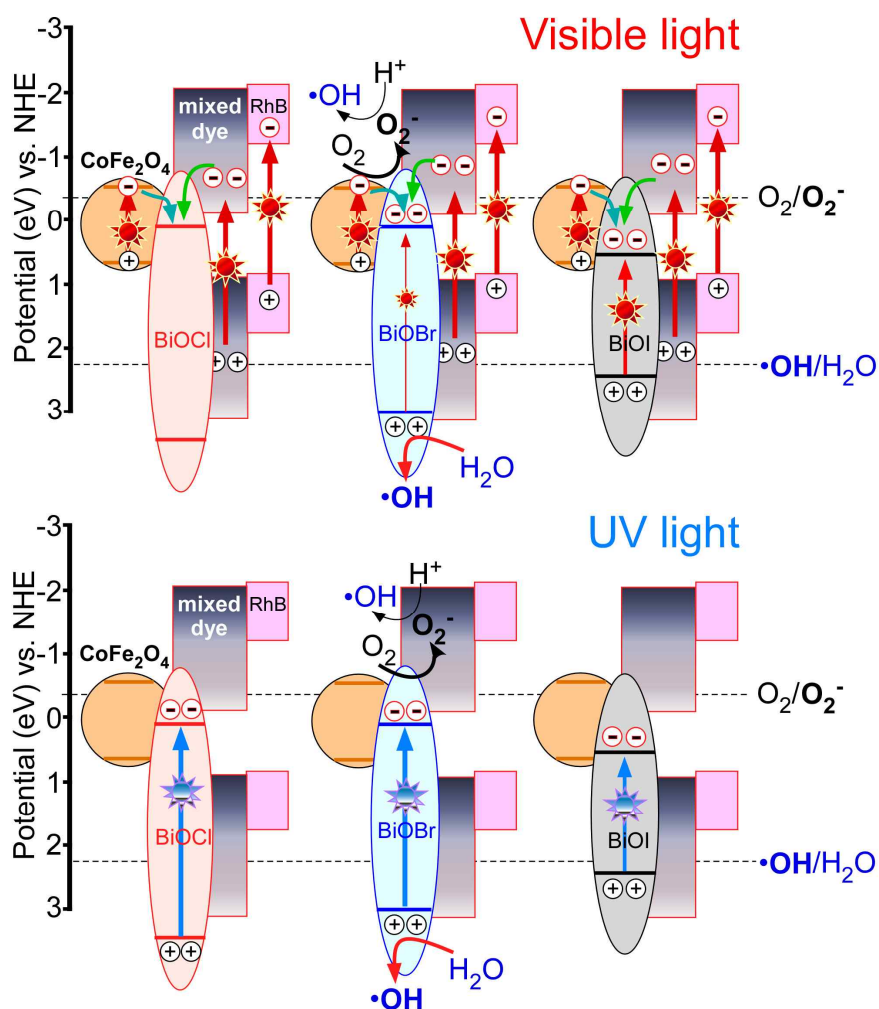


Figure 14. Photocatalytic dye degradation mechanism of a dye over the $\text{CoFe}_2\text{O}_4/\text{BiOX}$ (X= Cl, Br and I) microflowers. The red and blue vertical arrows indicate direct UV and visible light absorptions, respectively.

4. Conclusion

Highly efficient recyclable magnetic $\text{CoFe}_2\text{O}_4/\text{BiOX}$ ($X=\text{Cl}$, Br and I) microflower photocatalysts were prepared by a solvothermal method and tested with a mixed dye ($\text{MO} + \text{RhB} + \text{MB}$) and pure MO , RhB and MB . The adsorption performance and photocatalytic activity of a photocatalyst for a complicated polluted system were examined. Several new important results are listed below.

1) A saturation magnetization of $62.3 \text{ emu} \cdot \text{g}^{-1}$ was measured for CoFe_2O_4 NPs. The magnetization values were decreased by $8 \sim 10\times$ upon hybridization.

2) For the adsorption of RhB , the adsorption performance showed an order of $\text{CoFe}_2\text{O}_4/\text{BiOBr} < \text{CoFe}_2\text{O}_4/\text{BiOCl} \ll \text{CoFe}_2\text{O}_4/\text{BiOI}$. The adsorption capacity of $\text{CoFe}_2\text{O}_4/\text{BiOI}$ was $160 \text{ mg/g}_{\text{cat}}$, which is much larger than $<5 \text{ mg/g}_{\text{cat}}$ for $\text{CoFe}_2\text{O}_4/\text{BiOCl}$ and $\text{CoFe}_2\text{O}_4/\text{BiOBr}$.

3) For the photocatalytic activity of pure RhB over $\text{CoFe}_2\text{O}_4/\text{BiOX}$ microflowers, the photocatalytic activity showed an order of $\text{CoFe}_2\text{O}_4/\text{BiOBr} < \text{CoFe}_2\text{O}_4/\text{BiOCl} < \text{CoFe}_2\text{O}_4/\text{BiOI}$.

4) The adsorption capacities of $\text{CoFe}_2\text{O}_4/\text{BiOI}$ for MO and MB were 24 and 21 mg/g_{cat} , respectively. For pure MO and MB , the adsorption and photocatalytic degradation performances showed orders of $\text{CoFe}_2\text{O}_4/\text{BiOCl} < \text{CoFe}_2\text{O}_4/\text{BiOBr} < \text{CoFe}_2\text{O}_4/\text{BiOI}$ and $\text{CoFe}_2\text{O}_4/\text{BiOBr} < \text{CoFe}_2\text{O}_4/\text{BiOCl} < \text{CoFe}_2\text{O}_4/\text{BiOI}$, respectively.

5) The adsorptions in the mixed dye were different. In the mixed dye, MB showed the best adsorption over the $\text{CoFe}_2\text{O}_4/\text{BiOI}$ microflowers while MO showed the best adsorption over the $\text{CoFe}_2\text{O}_4/\text{BiOCl}$ and $\text{CoFe}_2\text{O}_4/\text{BiOBr}$ microflowers. On the other hand, RhB was the most poorly adsorbed on the $\text{CoFe}_2\text{O}_4/\text{BiOX}$ microflowers.

6) The degradation rate of each dye in the mixed system was different. The MO dye was removed most easily by the catalysts under UV and visible light exposure. $\text{CoFe}_2\text{O}_4/\text{BiOBr}$ showed the highest photocatalytic activity for MO degradation while $\text{CoFe}_2\text{O}_4/\text{BiOI}$ showed the highest activity for RhB and MB degradation.

7) For $\text{CoFe}_2\text{O}_4/\text{BiOX}$ microflowers, h^+ and $\bullet\text{O}_2^-$ play major and minor roles in photodegradation of the dyes, respectively. Although the $\bullet\text{OH}$ radical was formed for $\text{CoFe}_2\text{O}_4/\text{BiOBr}$ and $\text{CoFe}_2\text{O}_4/\text{BiOCl}$ under visible light, the role was found to be negligible. No $\bullet\text{OH}$ radical was formed for $\text{CoFe}_2\text{O}_4/\text{BiOI}$ both under UV and visible

light irradiations.

The newly developed magnetic photocatalysts provide new insights into the design of recyclable adsorbents and photocatalysts for a more complicated polluted system.

Acknowledgements. This study was supported financially by the National Research Foundation of Korea (NRF) grant funded by the Korean government (MEST) (NRF-2014R1A1A2055923).

References

1. L. Ye, Y. Su, X. Jin and H. Xie, C. Zhang, *Environ. Sci.: Nano*, 2014, **1**, 90–112.
2. H. Cheng, B. Huang and Y. Dai, *Nanoscale*, 2014, **6**, 2009-2026.
3. H. Zhao, F. Tian, R. Wang and R. Chen, *Rev. Adv. Sci. Eng.*, 2014, **3**, 3-27.
4. J. Li, Y. Yu and L. Zhang, *Nanoscale*, 2014, **6**, 8473-8488.
5. L. Zhang, W. Wang, S. Sun, Y. Sun, E. Gao and J. Xu, *Appl. Catal. B*, 2013, **132-133**, 315-320.
6. K. Li, Y. Tang, Y. Xu, Y. Wang, Y. Huo, H. Li and J. Jia, *Appl. Catal. B*, 2013, **140-141**, 179-188.
7. J. Xiong, G. Cheng, F. Qin, R. Wang, H. Sun and R. Chen, *Chem. Eng. J.*, 2013, **220**, 228-236.
8. Hu, S. Weng, Z. Zheng, Z. Pei, M. Huang and P. Liu, *J. Hazard. Mater.*, 2014, **264**, 293–302.
9. S. Wang, L. Wang, W. Ma, D. Johnson, Y. Fang, M. Jia and Y. Huang, *Chem. Eng. J.*, 2015, **259**, 410–416.
10. L. Ai, Y. Zeng and J. Jiang, *Chem. Eng. J.*, 2014, **235**, 331–339.
11. W. Kim, D. Pradhan, B. Min and Y. Sohn, *Appl. Catal. B*, 2014, **147**, 711-725.
12. Y. Park, Y. Na, D. Pradhan, B. Min and Y. Sohn, *CrystEngComm*, 2014, **16**, 3155–3167.
13. X. Zhang, X. Liu, C. Fan, Y. Wang, Y. Wang and Z. Liang, *Appl. Catal. B*, 2013, **132-133**, 332-341.
14. H. Cheng, B. Huang, X. Qin, X. Zhang and Y. Dai, *Chem. Commun.*, 2012, **48**, 97-99.

15. C. Zheng, C. Cao and Z. Ali, *Phys. Chem. Chem. Phys.*, 2015, **17**, 13347-13354.
16. L. Ye, J. Liu, Z. Jiang, T. Peng and L. Zan, *Appl. Catal. B*, 2013, **142-143**, 1-7.
17. C. Yu, F. Cao, G. Li, R. Wei, J. Yu, R. Jin, Q. Fan and C. Wang, *Sep. Sci. Technol.*, 2013, **120**, 110-122.
18. L. Lu, L. Kong, Z. Jiang, H. Lai, T. Xiao and P. Edwards, *Catal. Lett.*, 2012, **142**, 771-778.
19. T. Li, S. Luo and L. Yang, *J. Solid State Chem.*, 2013, **206**, 308-316.
20. Y. Lei, G. Wang and P. Guo, H. Song, *Appl. Surf. Sci.*, 2013, **279**, 374-379.
21. F. Li, Q. Wang, X. Wang, B. Li, Y. Hao, R. Liu and D. Zhao, *Appl. Catal. B*, 2014, **150-151**, 574-584.
22. H. Li, Y. Cui and W. Hong, *Appl. Surf. Sci.*, 2013, **264**, 581-588.
23. X. Zhang, T. Guo, X. Wang, Y. Wang, C. Fan and H. Zhang, *Appl. Catal. B*, 2014, **150-151**, 486-495.
24. J. Cao, B. Xu, H. Lin and S. Chen, *Chem. Eng. J.*, 2013, **228**, 482-488.
25. Z. Cui, M. Si, Z. Zheng, L. Mi, W. Fa and H. Jia, *Catal. Commun.*, 2013, **42**, 121-124.
26. C. Chang, L. Zhu, Y. Fu and X. Chu, *Chem. Eng. J.*, 2013, **233**, 305-314.
27. M. Su, C. He, L. Zhu, Z. Sun, C. Shan, Q. Zhang, D. Shu, R. Qiu and Y. Xiong, *J. Hazard. Mater.*, 2012, **229-230**, 72-82.
28. X. Wei, H. Cui, S. Guo, L. Zhao and W. Li, *J. Hazard. Mater.*, 2013, **263**, 650-658.
29. R. Wang, G. Jiang, X. Wang, R. Hu, X. Xi, S. Bao, Y. Zhou, T. Tong, S. Wang, T. Wang and W. Chen, *Powder Technol.*, 2012, **228**, 258-263.
30. X. Zhang, X. Chang, M. Gondal, B. Zhang, Y. Liu and G. Ji, *Appl. Surf. Sci.*, 2012, **258**, 7826-7832.
31. Z. Wu, W. Li, P.A. Webley and D. Zhao, *Adv. Mater.*, 2012, **24**, 485-491.
32. T. Xie, L. Xu, C. Liu, J. Yang and M. Wang, *Dalton Trans.*, 2014, **43**, 2211-2220.
33. Y. Yao, W. Huang, H. Zhou, Y. Zheng and X. Song, *J. Nanopart. Res.*, 2014, **16**, 2451-2459.
34. L. Zhang, W. Wang, S. Sun, Y. Sun, E. Gao and Z. Zhang, *Appl. Catal. B*, 2014, **148-149**, 164-169.

35. L. Zhang, W. Wang, L. Zhou, M. Shang and S. Sun, *Appl. Catal. B*, 2009, **90**, 458–462.
36. C. Tan, G. Zhu, M. Hojamberdiev, C. Xu, J. Liang, P. Luo and Y. Liu, *J. Clust. Sci.*, 2013, **24**, 1115–1126.
37. Y. Yao, W. Huang, H. Zhou, H. Yin, Y. Zheng and X. Song, *Mater. Chem. Phys.*, 2014, **148**, 896–902.
38. C. Guo, Y. He, P. Du, X. Zhao, J. Lv, W. Meng, Y. Zhang and J. Xu, *Appl. Surf. Sci.*, 2014, **320**, 383–390.
39. L. Kong, Z. Jiang, T. Xiao, L. Lu, M. Jones and P. Edwards, *Chem. Commun.*, 2011, **47**, 5512–5514.
40. X. Li, C. Niu, D. Huang, X. Wang, X. Zhang, G. Zeng and Q. Niu, *Appl. Surf. Sci.*, 2013, **286**, 40–46.
41. J. Xu, W. Meng, Y. Zhang, L. Li and C. Guo, *Appl. Catal. B*, 2011, **107**, 355–362.
42. J. Xu, L. Li, C. Guo, Y. Zhang and W. Meng, *Appl. Catal. B*, 2013, **130–131**, 285–292.
43. X. Wang, W. Yang, F. Li, J. Zhao, R. Liu, S. Liu and B. Li, *J. Hazard. Mater.*, 2015, **292**, 126–136.
44. M. Kooti and E. Nasiri, *J. Mol. Catal. A*, 2015, **406**, 168–177.
45. Z. Cai, Y. J. Liu, X. Lu and J. Teng, *J. Phys. Chem. C*, 2013, **117**, 9440–9445.
46. Z. Cai, J. Teng, Z. Xiong, Y. Li, Q. Li, X. Lu and X. S. Zhao, *Langmuir*, 2011, **27**, 5157–5164.
47. B. Tian, T. Wang, R. Dong, S. Bao, F. Yang and J. Zhang, *Appl. Catal. B*, 2014, **147**, 22–28.
48. Z. Cai, Z. Xiong, X. Lu and J. Teng, *J. Mater. Chem. A*, 2014, **2**, 545–553.
49. J. Cao, B. Xu, H. Lin, B. Luo and S. Chen, *Chem. Eng. J.*, 2012, **185–186**, 91–99.
50. M. Yin, Z. Li, J. Kou and Z. Zou, *Environ. Sci. Technol.*, 2009, **43**, 8361–8366.
51. X. Qin, H. Cheng, W. Wang, B. Huang, X. Zhang, and Y. Dai, *Mater. Lett.*, 2013, **100**, 285–288.
52. J. Jiang, K. Zhao, X. Xiao and L. Zhang, *J. Am. Chem. Soc.*, 2012, **134**, 4473–4476.
53. D. Zhang, J. Li, Q. Wang and Q. Wu, *J. Mater. Chem. A*, 2013, **1**, 8622–8629.
54. Y. Li, J. Wang, H. Yao, L. Dang and Z. Li, *J. Mol. Catal. A*, 2011, **334**, 116–122.

55. K. Vignesh, A. Suganthi, B. Min and M. Kang, *Appl. Surf. Sci.*, 2015, **324**, 652–661.
56. C. Yu, F. Cao, G. Li, R. Wei, J. Yu, R. Jin, Q. Fan and C. Wang, *Sep. Purif. Technol.*, 2013, **120**, 110-122.
57. Y. I. Choi, H. J. Jung, W. G. Shin and Y. Sohn, *Appl. Surf. Sci.*, 2015, **356**, 615–625.
58. M. J. Kim, Y. I. Choi, S. W. Joo, M. Kang and Y. Sohn, *Ceram. Inter.*, 2014, **40**, 16051-16059.
59. Y. Na, Y. I. Kim, D. W. Cho, D. Pradhan and Y. Sohn, *Mater. Sci. Semicond. Process.*, 2014, **27**, 181-190.
60. N. Roy, Y. Park, Y. Sohn, K. T. Leung and D. Pradhan, *ACS Appl. Mater. Interfaces*, 2014, **6**, 16498-16507.
61. Y. Na, S. W. Lee, N. Roy, D. Pradhan and Y. Sohn, *CrystEngComm*, 2014, **16**, 8546-8554.
62. A. K. Nayak, S. Lee, Y. Sohn and D. Pradhan, *CrystEngComm*, 2014, **16**, 8064-8072.
63. M. M. Khan, S. A. Ansari, M. O. Ansari, B. K. Min, J. Lee and M. H. Cho, *J. Phys. Chem. C*, 2014, **118**, 9477–9484.
64. B. Holinsworth, D. Mazumdar, H. Sims, Q. Sun, M. Yurtisigi, S. Sarker, A. Gupta, W. Butler and J. Musfeldt, *Appl. Phys. Lett.*, 2013, **103**, 082406-082409.
65. Ye, L. Tian, T. Peng and L. Zan, *J. Mater. Chem.*, 2011, **21**, 12479-12484.